Supporting Information

Dynamically Linking Influenza Virus Infection with Lung Injury to Predict Disease Severity

Margaret A. Myers[1], Amanda P. Smith[1], Lindey C. Lane[1], David J. Moquin[2], Peter Vogel[3], Stacie Woolard[4], and Amber M. Smith[1,*]

[1] Department of Pediatrics, University of Tennessee Health Science Center, Memphis, TN 38163, USA

[2] Department of Anesthesiology, Washington University School of Medicine, St. Louis, MO 63110 USA

[3] Department of Pathology, St. Jude Children's Research Hospital, Memphis, TN 38105, USA

[4] Flow Cytometry Core, St. Jude Children's Research Hospital, Memphis, TN 38105, USA

* amber.smith@uthsc.edu

Alternate CD8$^+$ T cell Model

We examined an alternate formulation of the CD8$^+$ T cell model to further investigate the density-dependence in the CD8$^+$ T cell response. Rather than assuming that CD8$_\mathrm{E}$-mediated clearance of infected cells is dependent on their density, the model in Equations (S1)–(S6) assumes that the rate of CD8$_\mathrm{E}$ expansion is dependent on the density of infected cells. Similar models have been used to study CD8$^+$ T cell responses during HIV infection [1, 2] and other viral infections [3]. The differences of this alternate model from the CD8$^+$ T cell model (Equations (1)–(6); Main Text) are in bold.

$$\frac{dT}{dt} = -\beta TV \tag{S1}$$

$$\frac{dI_1}{dt} = \beta TV - kI_1 \tag{S2}$$

$$\frac{dI_2}{dt} = kI_1 - \delta I_2 - \delta_{\mathbf{Ea}}\mathbf{E}\mathbf{I_2} \tag{S3}$$

$$\frac{dV}{dt} = pI_2 - cV \tag{S4}$$

$$\frac{dE}{dt} = \frac{\eta_{\mathbf{Ea}}}{\mathbf{K_{Ea}} + \mathbf{I_2}} EI_2(t-\tau_E) - d_E E \tag{S5}$$

$$\frac{dE_M}{dt} = \zeta E(t-\tau_M) \tag{S6}$$

When a linear CD8$_\mathrm{E}$-mediated infected cell clearance rate is included, the CD8$_\mathrm{E}$ dynamics between 3–5 d pi cannot be replicated. However, because these cells may not have effector functions and contribute to infected cell clearance at this time (see Discussion in Main Text), we excluded these data and the term $\xi I_2/(K_E+E)$ when fitting Equations (S1)–(S6) to the viral load and CD8$^+$ T cell data (Figure S1). The model dynamics are similar to those generated by CD8$^+$ T cell model in the Main Text. However, the alternate model slightly underestimates the data at day 7 and the sharp decline between 7–8 d. The two models cannot be compared statistically due to the varying number of data points.

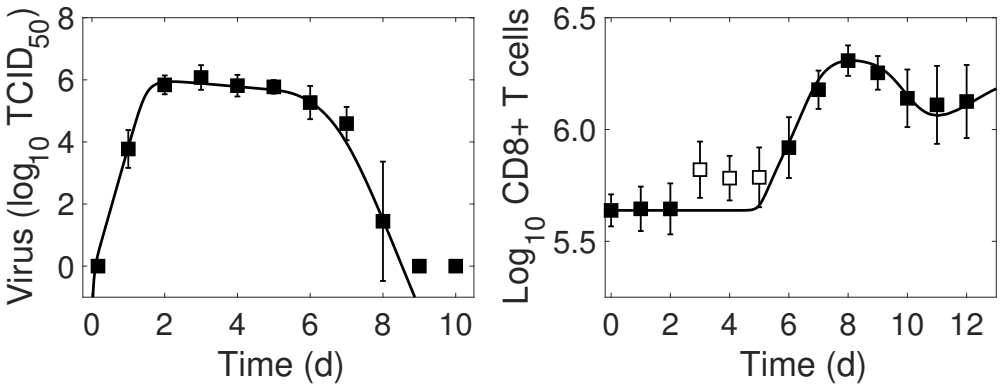

Figure S1. Fit of an Alternate CD8$^+$ T cell Model. Fit of an alternate CD8$^+$ T cell model (Equations (S1)–(S6)) to virus and CD8$^+$ T cells (excluding 3–5 d pi; white squares) from the lungs of mice infected with 75 TCID$_{50}$ PR8 (10 mice per time point). The total number of CD8$^+$ T cells is $\hat{E} = E + E_M + \hat{E}_0$. Resulting parameter values were $\delta_{Ea} = 4.02 \times 10^6$, $\eta_{Ea} = 3.12 \times 10^5$, and $K_{Ea} = 9.53 \times 10^5$. All other parameters are in Table 1. Data are shown as mean ± standard deviation.

Additional Parameter Ensembles

Figures S2–S3 show parameter ensembles obtained from fitting the CD8$^+$ T cell model (Equations (1)–(6)) simultaneously to viral titers and CD8$^+$ T cells from BALB/cJ mice infected with 75 TCID$_{50}$ PR8. All other parameter ensembles are shown in Figure 2 (Main Text).

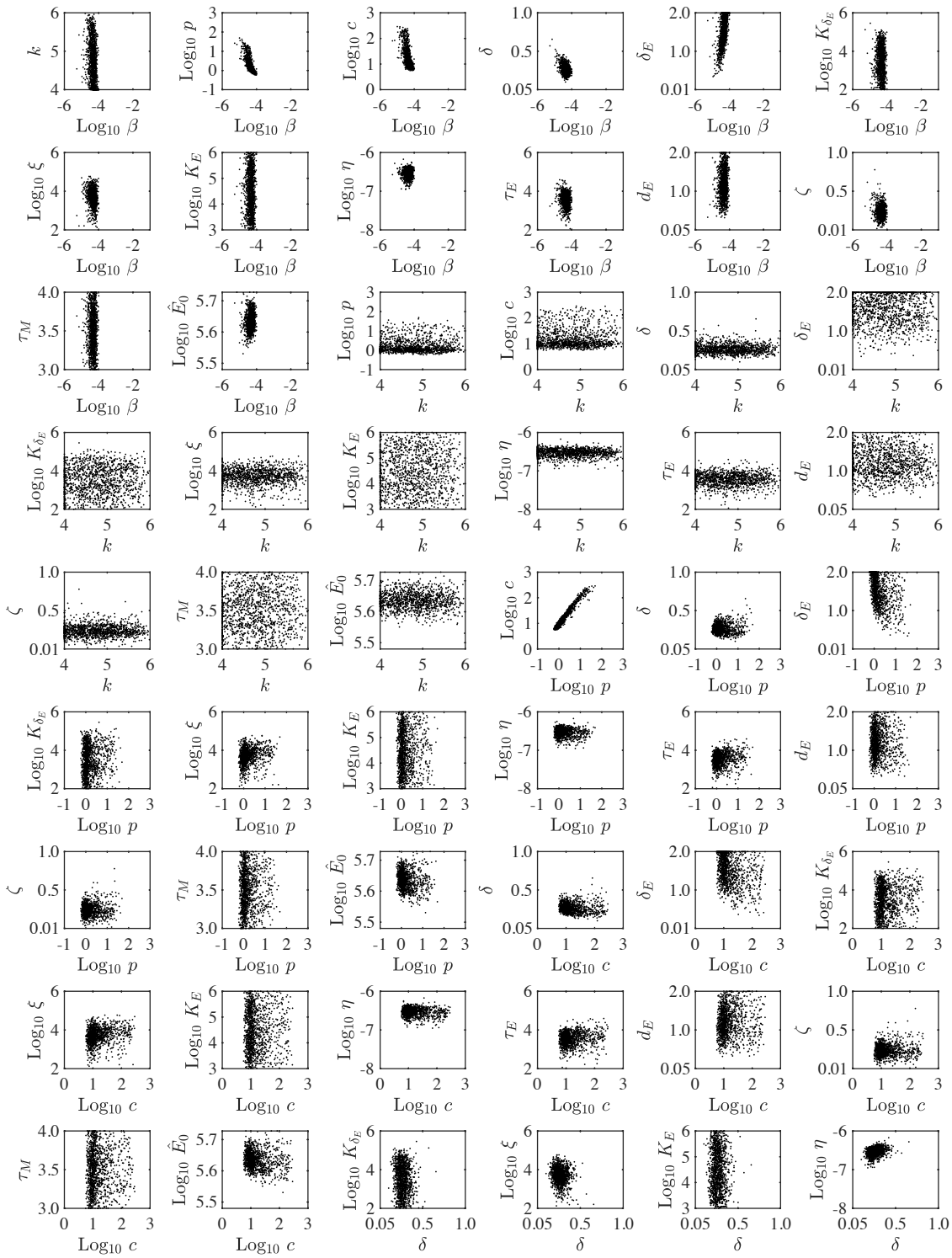

Figure S2. Parameter Ensembles. Parameter ensembles resulting from fitting the CD8$^+$ T cell model (Equations (1)–(6), Main Text) to viral loads and CD8$^+$ T cells from mice infected with 75 TCID_{50} PR8. The axes limits reflect the imposed bounds. Additional ensemble plots are in Figure 2 (Main Text) and Figure S3.

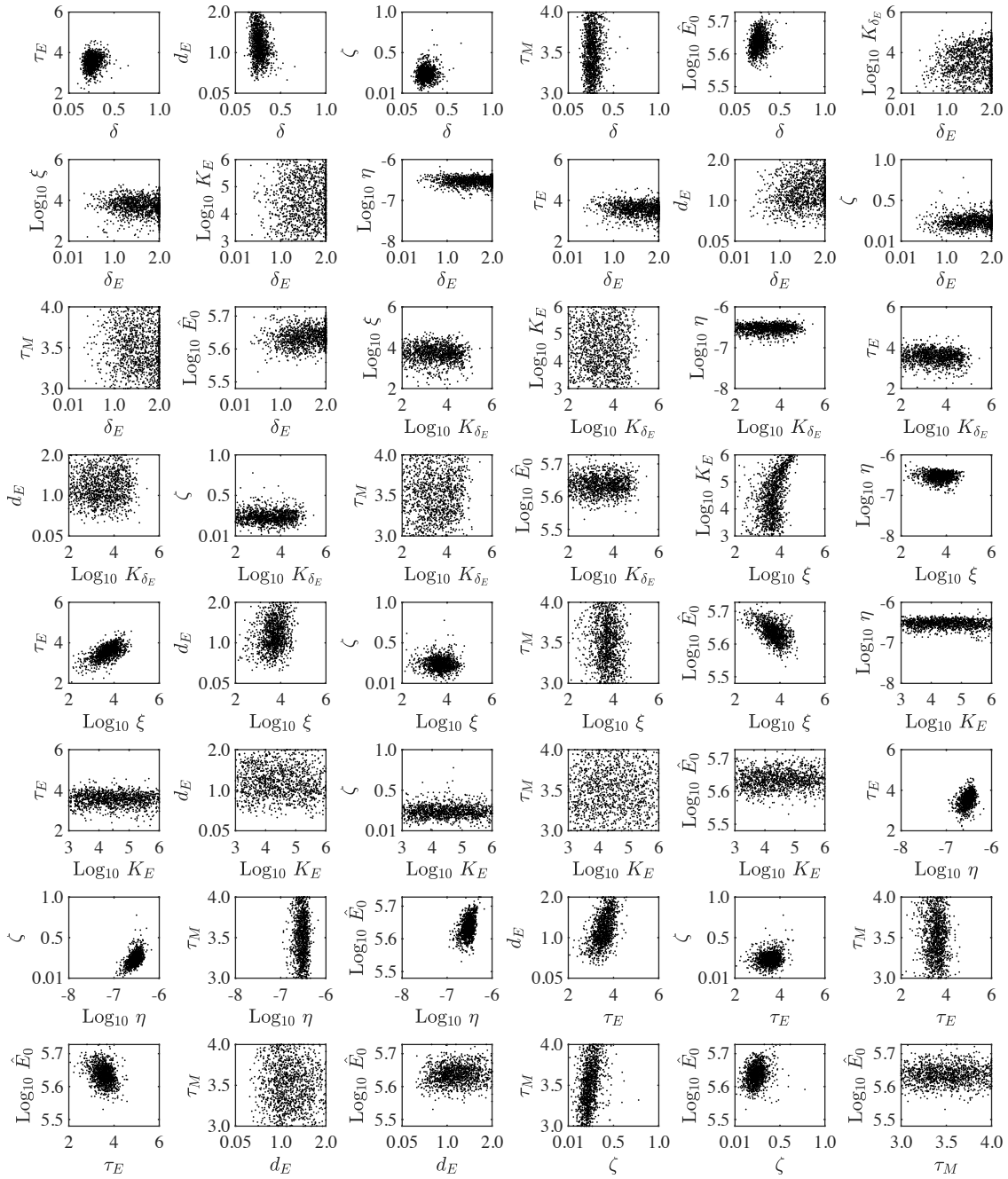

Figure S3. Parameter Ensembles. Parameter ensembles resulting from fitting the CD8$^+$ T cell model (Equations (1)–(6), Main Text) to viral loads and CD8$^+$ T cells from mice infected with 75 TCID_{50} PR8. The axes limits reflect the imposed bounds. Additional ensemble plots are in Figure 2 (Main Text) and Figure S2.

Comparison of the Density-Dependent and CD8$^+$ T cell Models

We previously developed a density-dependent (DD) viral kinetic model, which describes the biphasic decline of viral loads without inclusion of specific host responses [4]. This model tracks 4 populations: susceptible epithelial ("target") cells (T), two classes of infected cells (I_1 and I_2), and virus (V) [4].

$$\frac{dT}{dt} = -\beta TV \tag{S7}$$

$$\frac{dI_1}{dt} = \beta TV - kI_1 \tag{S8}$$

$$\frac{dI_2}{dt} = kI_1 - \delta_d(I_2)I_2 \tag{S9}$$

$$\frac{dV}{dt} = pI_2 - cV \tag{S10}$$

Briefly, in the DD model, virus-producing infected cells (I_2) are cleared according to the function $\delta_d(I_2) = \delta_d/(K_\delta + I_2)$, where δ_d/K_δ is the maximum per day rate of infected cell clearance and K_δ is the half-saturation constant (Figure S4). All other terms are common to the CD8 T$^+$ cell model (Equations (1)–(6), Main Text). The DD model provides a close fit to the viral load data in Figure 1B and replicates the biphasic viral load decline while excluding the dynamics of specific immune responses [4]. Unsurprisingly, the CD8$^+$ T cell model is also capable of reproducing the biphasic viral load decay (Figure 1B and S4). In that model, infected cell clearance is split into terms for non-specific clearance (δ) and CD8$_\mathrm{E}$-mediated clearance ($\delta_E(I_2, E) = \delta_E E/(K_\delta + I_2)$) (Figure S4).

Because the CD8$^+$ T cell model is more mechanistic than the DD model, most of the correlations between the parameters common to both models (i.e., the rates of virus infectivity (β), virus production (p), and virus clearance (c)) were reduced (Figure S4A). In addition, the correlations between the infected cell clearance parameters (δ_d and K_δ or δ_E and K_{δ_E}) and between the rate of virus infectivity (β) and their ratios (δ_d/K_δ or δ_E/K_{δ_E}) were abolished (Figures S2–S3). There was a negative correlation between the infected cell clearance parameters (δ and δ_E; Figure 2B), which may reflect the connection between the efficacy of early immune mechanisms and the CD8$^+$ T cell response. This result is in line with experimental evidence that the innate immune responses modulate the activation of adaptive immunity [5–9].

The differences in model structure between the two models yielded changes in parameter sensitivity and model behavior during the rapid viral clearance phase (Figure S4). In the DD model, the most sensitive parameter is the infected cell clearance, δ_d (Figure S4). A 50% decrease in this parameter resulted in a ∼7 d delay in viral resolution (Figure S4) [4]. In the CD8$^+$ T cell model, however, viral resolution is delayed by <1 d if the CD8$_\mathrm{E}$-mediated infected cell clearance parameter (δ_E) is reduced by 50% (Figures S4–S5). The rates of CD8$_\mathrm{E}$ expansion (η) and decay (d_E) are sensitive and, thus, significantly influence the viral resolution kinetics (Figures S4–S6). A 50% decrease in η results in a ∼6 d delay in recovery (Figures S4–S5) whereas a 48% decrease in η prolongs the infection by ∼30 d (Figure 3D–E). This bifurcation in recovery time is a unique feature of the CD8$^+$ T cell model (discussed in the Main Text).

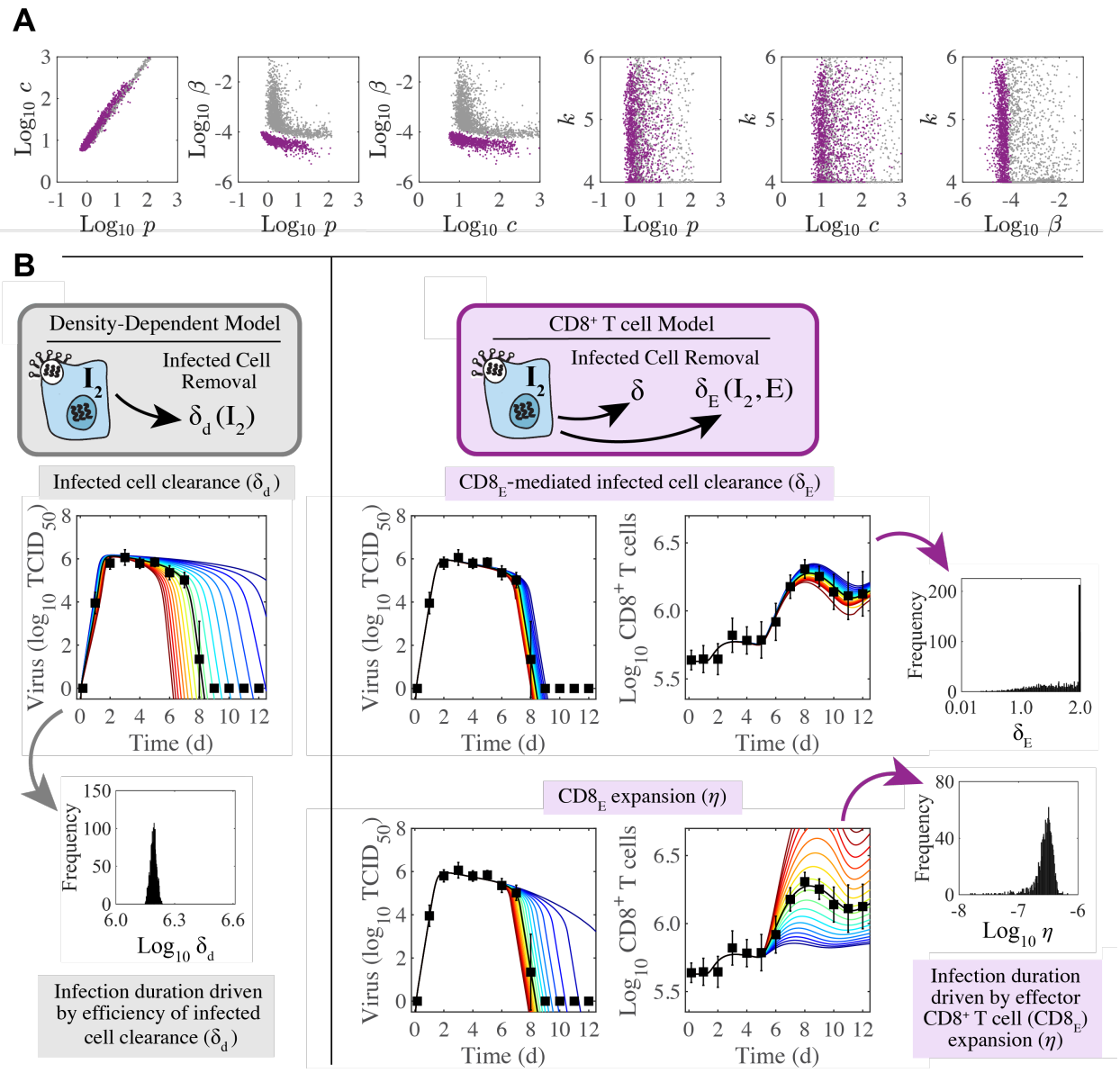

Figure S4. Parameter behavior of the density-dependent model and the CD8$^+$ T cell model. (A) Comparison of parameters that were common between the density-dependent model (gray, Equations (S7)–(S10)) and the CD8$^+$ T cell model (purple, Equations (1)-(6), Main Text). Correlations were evident between parameters relating to the rates of virus infectivity (β), virus production (p), and virus clearance (c). However, the strength of the correlation was significantly reduced in the CD8$^+$ T cell model. The eclipse phase parameter (k) was not well-defined in either model. (B) In the density-dependent model (gray), the viral kinetics and the infection duration were sensitive to small changes in the infected cell clearance parameter (δ_d). This parameter was well-defined with a narrow 95% CI. In the CD8$^+$ T cell model (purple), changing the CD8$_E$-mediated infected cell clearance parameter (δ_E) had little impact on viral kinetics or CD8$^+$ T cell kinetics. However, these kinetics were most sensitive to changes in the rate of CD8$_E$ expansion (η), which was well-defined with a narrow 95% CI.

Regulation of the CD8$^+$ T cell Response

To further understand the regulation of the CD8$^+$ T cell response, we examined the 2-D parameter ensembles (Figure 2A–C, Figures S2–S3) and the results from the sensitivity analysis (Figure S5–S6). Overall, few parameters were correlated. There was an expected, although small, positive correlation between the rate of $CD8_E$ infiltration (ξ) and the associated half-saturation constant (K_E) (Figure S3), which represents the coordination between $CD8_E$ recruitment and the processes that prevent an overabundance of these cells. Likewise, a negative correlation was detected between the rate of $CD8_E$ infiltration (ξ) and the initial number of CD8$^+$ T cells ($\hat{E}_0$) (Figure S3). The infiltration rate (ξ) was also positively correlated with the delay in $CD8_E$ expansion (τ_E) (Figure S3). The rates of $CD8_E$ expansion (η) and decay (d_E) are correlated (Figure 2C, Main Text), indicating a balance between these two processes. This correlation was expected and reflects the coordination of mechanisms that regulate CD8$^+$ T cell numbers, which may be necessary to limit excessive immunopathology while still resolving the infection [10–12]. Further, because of this correlation and the sensitivity of η (Figure S5), the CD8$^+$ T cell kinetics are sensitive to changes in d_E (Figure S6). However, increasing the decay rate had less impact on the viral load kinetics, comparatively. Because d_E is correlated with both η and the rate of $CD8_M$ generation (ζ) (Figure 2C), it naturally follows that η and ζ are correlated (Figure S3). Changing the rates of virus infectivity (β), production (p), or clearance (c) had little effect on viral load or CD8$^+$ T cell kinetics (Figure S5).

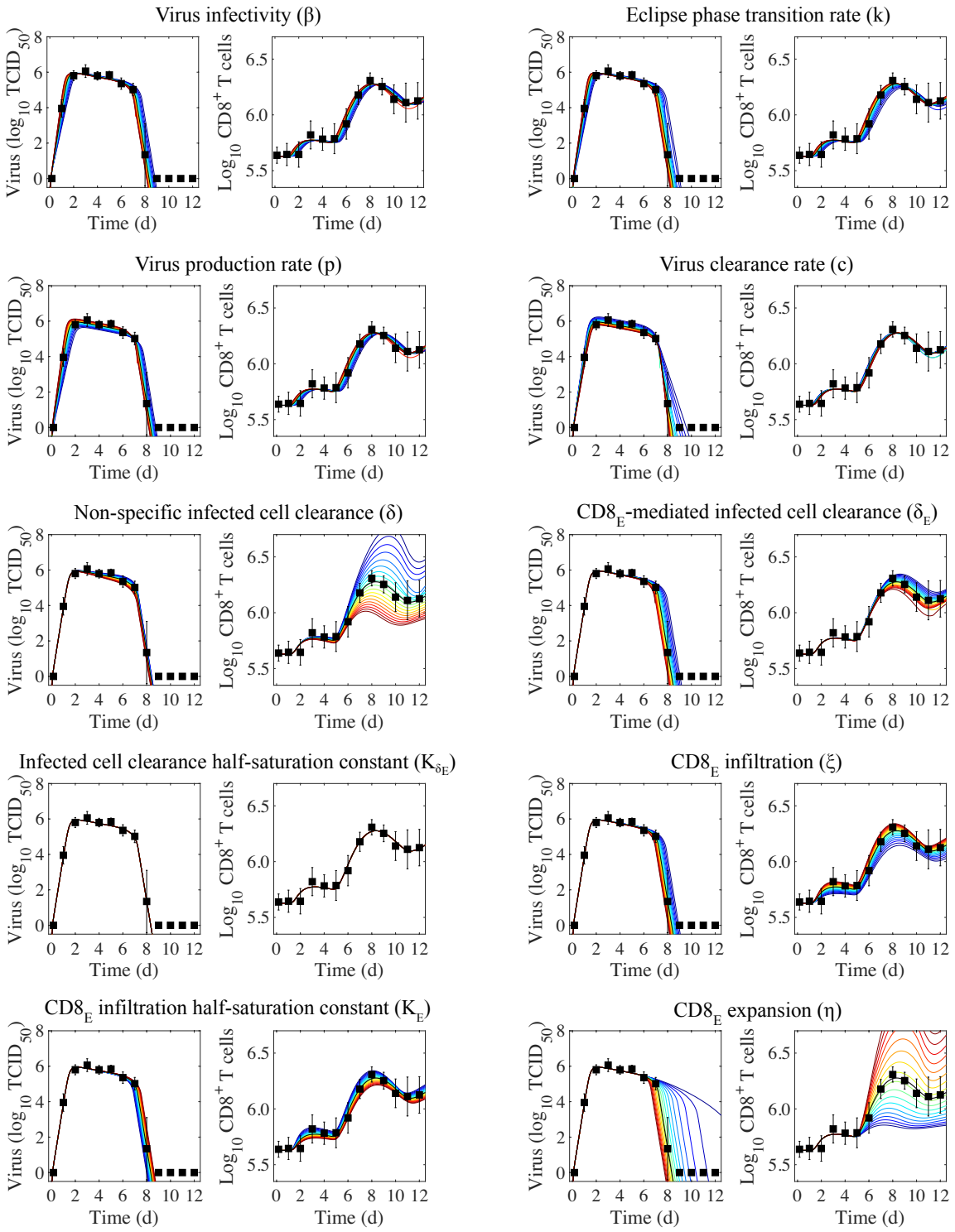

Figure S5. Sensitivity of the CD8$^+$ T cell model. Solutions of the CD8$^+$ T cell model (Equations (1)–(6); Main Text) with the indicated parameter (β, k, p, c, δ, δ_E, K_{δ_E}, ξ, K_E, or η) increased (red) or decreased (blue) 50% from the best-fit value (Table 1, Main Text). $CD8_E$ denotes effector CD8$^+$ T cells.

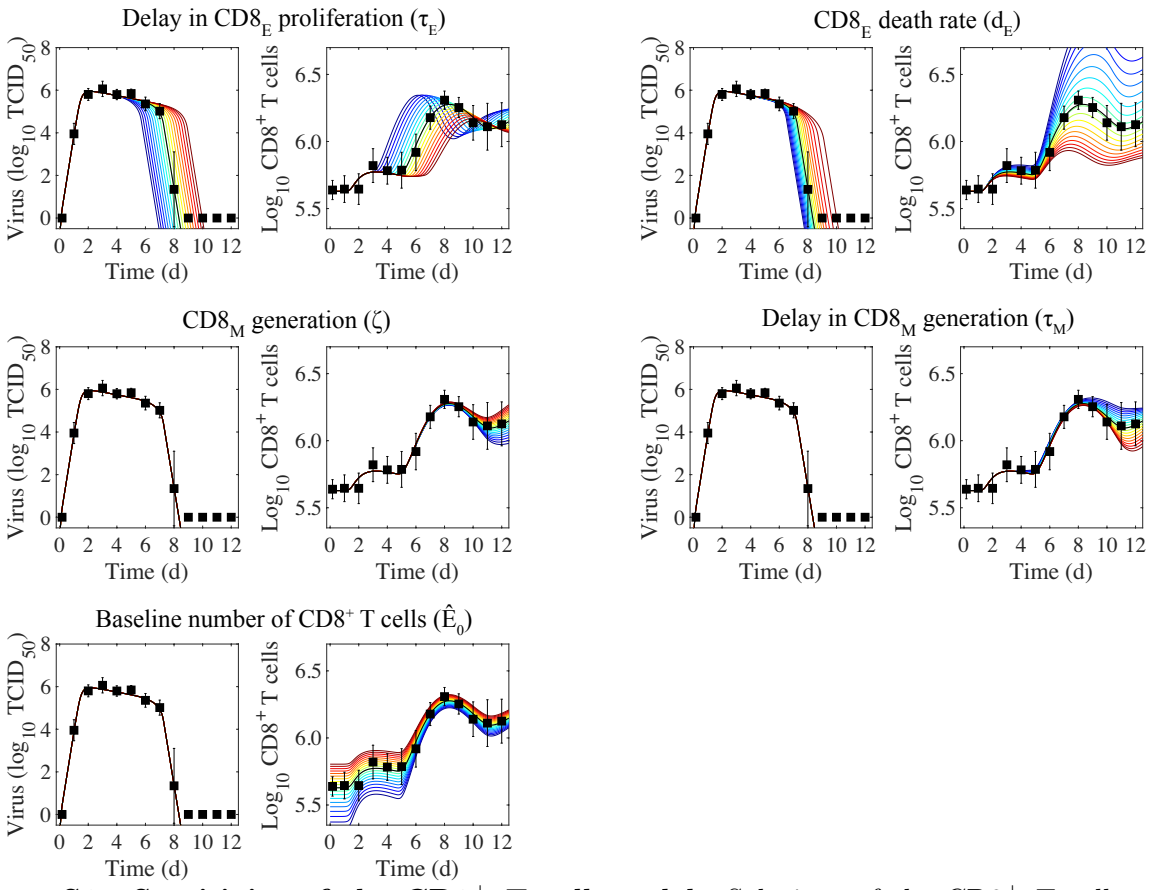

Figure S6. Sensitivity of the CD8$^+$ T cell model. Solutions of the CD8$^+$ T cell model (Equations (1)–(6); Main Text) with the indicated parameter (τ_E, d_E, ζ, τ_M, or $\hat{E}_0$) increased (red) or decreased (blue) 50% from the best-fit value (Table 1, Main Text). $CD8_E$ and $CD8_M$ denote effector and memory CD8$^+$ T cells, respectively.

Linear Analysis of Lung Injury Dynamics

To further analyze the whole lung histomorphometry data in Figure 4, we completed a linear regression on the percent active lesioned area, the percent inactive lesioned area, and the number of $CD8^+$ T cells using the function *polyfit* in MATLAB (Figure S7). The percent active lesion declines at a rate of -28.7%/d between 6–7 d pi. The percent inactive lesion increases at a rate of 14.6%/d between 5–8 d pi, which corresponds to the increase in $CD8^+$ T cells (4.7×10^5 cells/d). The percent inactive lesion and the $CD8^+$ T cells decline at rates of -14.5%/d and -3.3×10^5 cells/d, respectively.

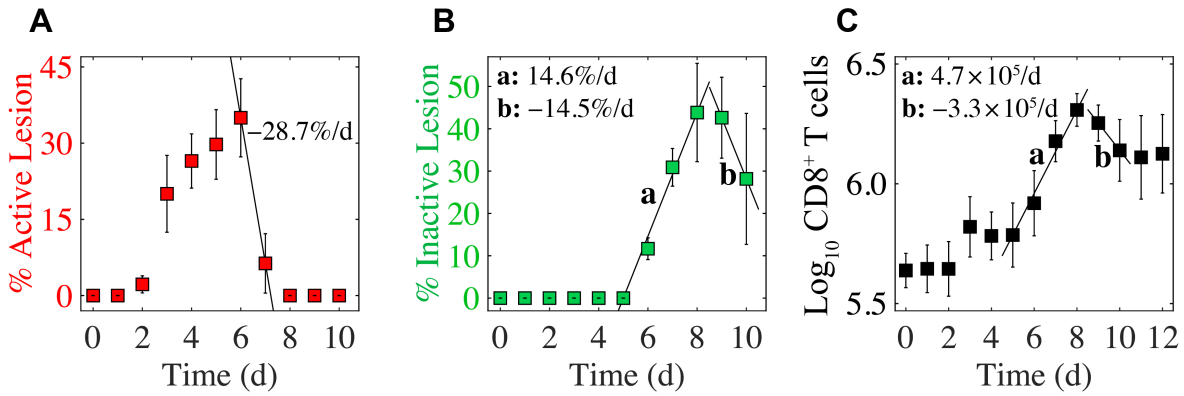

Figure S7. Linear regression analysis of lung injury dynamics and $CD8^+$ T cells. (A) Percent active lesion area decreases by 28.7%/d from 6–7 d pi. (B) Percent inactive lesion area increases by 14.6%/d from 5–8 d pi, and decreases by -14.5%/d from 9–10 d pi. (C) $CD8^+$ T cells increase at a rate of 4.7×10^5 cells/d (0.17 $\log_{10}$ cells/d) from 5–8 d pi, and decrease at a rate of -3.3×10^5 cells/d (-0.11 $\log_{10}$ cells/d) from 9–10 d pi.

Predicted Confidence Interval for the Total Lesion

Because the CAUC of the infected cells (I_2) and the relative $CD8_E$ of the model solution matched the kinetics and heterogeneity of the percent active and inactive lung lesions (Figure 4B–C, Main Text), we combined the two to estimate the total lesion (Figure S8). To include all measurements on the same scale, the linear decline in the active lesion (-28.7%/d; see Figure S7A) was used to estimate the decline after 6 d pi, the CAUC of I_2 was multiplied by a scaling factor of 14.2% per 10^7 cells, and the percent maximum $CD8_E$ was multiplied by a scaling factor of 0.46%.

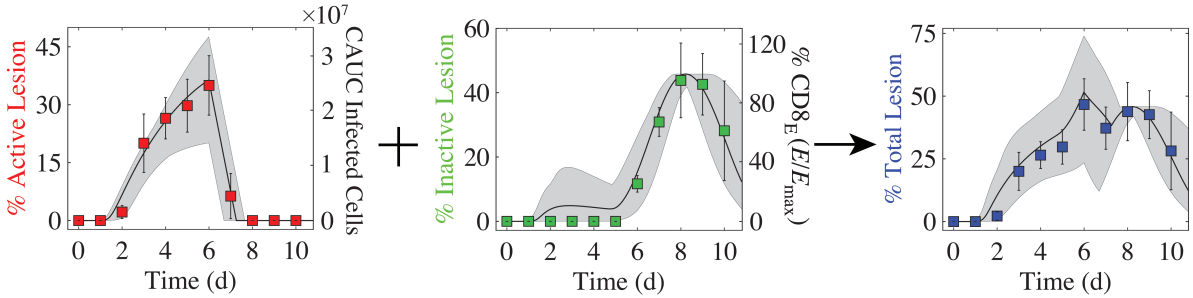

Figure S8. Predicted total lung lesion. The estimated active (red; CAUC of I_2) and inactive (green; percent maximum $CD8_E$) lesions generated using the best-fit parameters (black line) and the 95% CI parameters (gray shading) (Table 1, Main Text). The total lesion (blue) is the addition of the active and inactive lesions. To include all measurements on the same scale, the linear decline in the active lesion (-28.7%/d; see Figure S7A) was used to estimate the decline after 6 d pi, the CAUC of I_2 was multiplied by a scaling factor of 14.2% per 1×10^7 cells, and the percent maximum $CD8_E$ was multiplied by a scaling factor of 0.46%.

Gating strategy for flow cytometric analysis

Figure S9 shows the gating strategy used to define $CD8^+$ T cells (Figure 1A in the Main Text). Data shown are from a representative naïve animal.

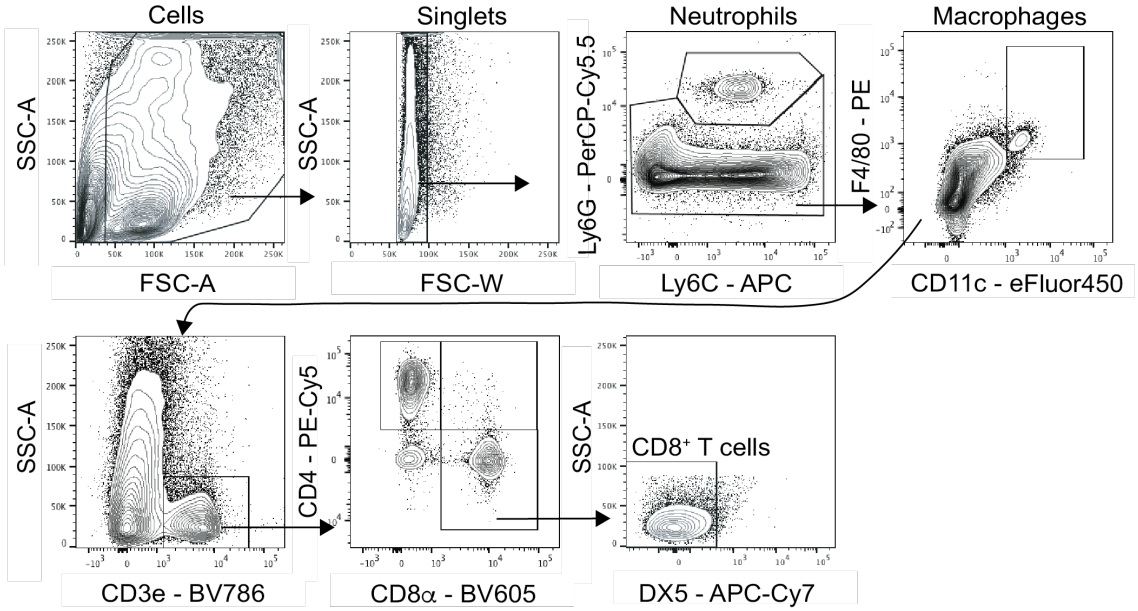

Figure S9. Flow cytometry gating strategy for $CD8^+$ T cell analysis. Live cells were first gated on forward scatter (FSC-A) and side scatter (SSC-A) then as singlets. Following neutrophil ($Ly6G^{hi}$) and macrophages ($CD11c^{hi}F4/80^{hi}$) exclusion, T cells were gated as $CD3e^+$ with $CD8^+$ T cells subgated as $CD8\alpha^+CD4^-DX5^-$.

References

1. Conway JM, Perelson AS. Post-treatment control of HIV infection. P Natl Acad Sci. 2015;112(17):5467–5472.

2. Bonhoeffer S, Rembiszewski M, Ortiz GM, Nixon DF. Risks and benefits of structured antiretroviral drug therapy interruptions in HIV-1 infection. Aids. 2000;14(15):2313–2322.

3. Baral S, Antia R, Dixit NM. A dynamical motif comprising the interactions between antigens and CD8 T cells may underlie the outcomes of viral infections. bioRxiv. 2019; p. 540054.

4. Smith AP, Moquin DJ, Bernhaurova V, Smith AM. Influenza virus infection model with density dependence supports biphasic viral decay. Front Microbiol. 2018;9:1554. doi:10.3389/fmicb.2018.01554.

5. Iwasaki A, Medzhitov R. Control of adaptive immunity by the innate immune system. Nat Immunol. 2015;16(4):343.

6. Luster AD. The role of chemokines in linking innate and adaptive immunity. Curr Opin Immunol. 2002;14(1):129–135.

7. Iwasaki A, Medzhitov R. Regulation of adaptive immunity by the innate immune system. Science. 2010;327(5963):291–295.

8. Le Bon A, Tough DF. Links between innate and adaptive immunity via type I interferon. Curr Opin Immunol. 2002;14(4):432–436.

9. Jain A, Pasare C. Innate control of adaptive immunity: Beyond the three-signal paradigm. J Immunol. 2017;198(10):3791–3800.

10. Moskophidis D, Kioussis D. Contribution of virus-specific $CD8^+$ cytotoxic T cells to virus clearance or pathologic manifestations of influenza virus infection in a T cell receptor transgenic mouse model. J Exp Med. 1998;188(2):223–232.

11. Duan S, Thomas PG. Balancing immune protection and immune pathology by $CD8^+$ T-cell responses to influenza infection. Front Immunol. 2016;7:25.

12. La Gruta NL, Kedzierska K, Stambas J, Doherty PC. A question of self-preservation: Immunopathology in influenza virus infection. Immunol Cell Biol. 2007;85(2):85–92.